Results in Physics 49 (2023) 106483

Contents lists available at ScienceDirect

Results in Physics

journal homepage: www.elsevier.com/locate/rinp

The ultra-high sensitivity of mass resonator achieved by the beam with variable thickness

Chenxi Wei [a,b], Yin Zhang [a,b,*]

[a] State Key Laboratory of Nonlinear Mechanics (LNM), Institute of Mechanics, Chinese Academy of Sciences, Beijing 100190, China
[b] School of Engineering Science, University of Chinese Academy of Sciences, Beijing 100049, China

ARTICLE INFO

Keywords:
Mass resonator
Sensitivity
Shape optimization
Resonant frequency
Beam
Variable thickness

ABSTRACT

The shift of resonant frequency due to the particle adsorption is the mass sensing mechanism of a micro/nano-resonator. The sensitivity and resolution are the two key performance indicators of a mass resonator. An effective method to significantly enhance the sensitivity of a mass resonator is presented. The method is realized by the design of the beam resonator thickness variation along the longitudinal direction. The analytical expression of the non-uniform resonator sensitivity and the optimization process on the thickness are given. The optimal shapes of the cantilevered and doubly clamped beam resonators are obtained by the optimization process. The sensitivities of the beam resonators in the optimal shapes are three orders of magnitude higher than those of the uniform ones. A systematic method of enhancing the sensitivity of a mass resonator through the shape optimization is thus provided. The influences of the axial load on the optimization results are also discussed.

Introduction

Micro/nano-resonators have been widely used in the particles sensing [1,2], materials detection [3,4] and environment sensing [5–7]. The mass resonators are the devices for the detection of the neutral, hazardous and biological matters [8–11]. The major advantages of a micro/nano-resonator are its ultra-high resonant frequency [12,13], throughput [14] and sensitivity [15]. Therefore, the mass resonators can be used to sense the extremely small particles, which reach atomic mass resolution [16].

By measuring the resonant frequencies before and after the particles adsorption, mass resonators can sense the particle mass with high efficiency and accuracy [17,18]. The sensitivity, which is also called the responsivity of the resonator [19], is an essential indicator of a resonator. The sensitivity is defined as the ratio of the resonant frequency shift to the attached mass [17]. The sensitivity expression for a uniform resonator is given as follows [19]:

$$s_j = \frac{\Delta\Omega_j}{m} = -\frac{\Omega_j}{2m_{eff}}\varphi_j^2(x_p). \tag{1}$$

here, m is the particle mass and x_p is the locus of particle; Ω_j and φ_j are the j-th resonant frequency and the corresponding mode shape of the resonator, respectively. The effective mass m_{eff} is defined as $m_{eff} = \rho bh\int_0^L \varphi_j^2(x)\mathrm{d}x$, where j is the mode number; ρ, b and h are the density, width and thickness of a uniform beam resonator, respectively. The resonant frequency $\Omega \propto \frac{h}{l^2}\sqrt{\frac{E}{\rho}}$ [20], where E is the Young's modulus and l is the length of a beam resonator. As indicated in Eq. (1) an effective way to achieve a high sensitivity for a beam resonator is to increase the resonant frequency, such as scaling down the resonators and using the materials with a larger Young's modulus and lower density [21]. However, scaling down the resonator will face the challenge of the nano-scaled fabrication on the nanostructures [22] and energy dissipation [23]. The high energy dissipation in nano-sized devices results in the low quality factor in the resonance measurements [24] and further affects the measuring resolution [25] and frequency noise [26] in the mass sensing. To mitigate this, the ultra-low temperature and pressure are recommended to reduce the dissipation and thus improve the quality factor [27]. Suspended microchannel resonator for weighing the biological samples like bacterial cells and adsorbed proteins, is developed in the vacuum environment with high sensitivity and quality factor [14]. The experiments show that a micro/nano-resonator will achieve a greater sensitivity when using a higher mode resonance to detect the attached particle [28,29]. The reason is that higher mode resonance can improve the resonant frequencies as shown in Eq. (1) and reduce the effective mass, without changing the physical dimensions of the

* Corresponding author at: State Key Laboratory of Nonlinear Mechanics (LNM), Institute of Mechanics, Chinese Academy of Sciences, Beijing 100190, China.
E-mail address: zhangyin@lnm.imech.ac.cn (Y. Zhang).

https://doi.org/10.1016/j.rinp.2023.106483
Received 15 February 2023; Received in revised form 17 April 2023; Accepted 20 April 2023
Available online 24 April 2023

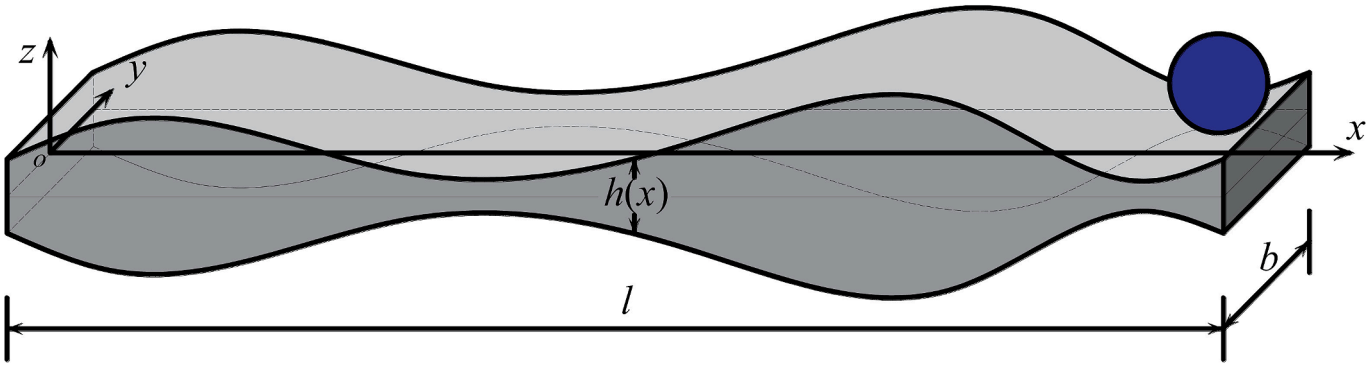

Fig. 1. Schematic diagram of a beam resonator with variable thickness.

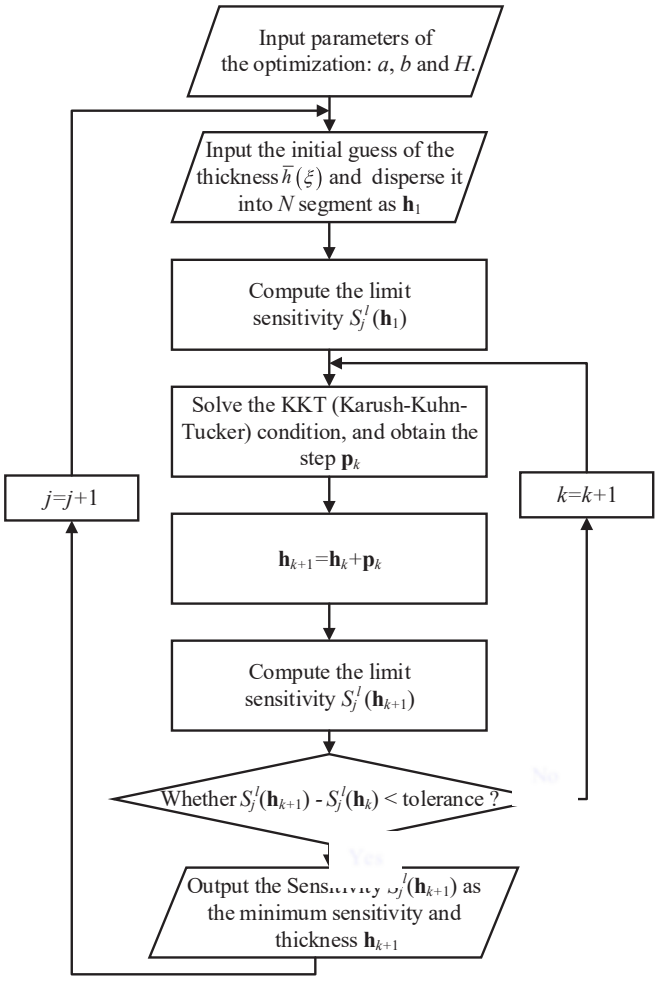

Fig. 2. Flowchart of the optimization procedures on beam thickness.

resonator [17]. Tensile stress on the resonator increases the resonant frequencies, which is effective to improve the sensitivity [30]. The tensile stress is also helpful to reduce the damping and improve the quality factor [19,31]. The resonator behaves like a string under the very large tension, which can be used for force sensing [32,33]. Because multiple particles increase the shift of resonant frequency, measuring multiple particles in mass sensing is a strategy to improve the sensitivity [34]. Using the mode localization in coupled micro-cantilevers can also improve the sensitivity on the added particle [35]. Furthermore, by adjusting the length and thickness of each layer, the sensitivity of the stepped cantilever resonator can be improved by almost twenty-fold [36].

Designing the shape is a practical method that improves the structure performance [37]. For the power harvesting, it is found that changing the width distribution of the beam can concentrate the strain in the section contributing most to the transduction, and thus improve the voltage output [38]. The vertical micro-pillars with the inverted tapered shape are designed and fabricated with the sensitivity of 33 Hz/fg (1 fg = 10^{-15} g) and the reproducibility of 0.1 fg [39]. By using the non-uniform beams array, the frequency bandwidth of the resonator is improved [40]. Adjusting the layers of the stepped beam can also be regarded as a shape design, which improves the sensitivity [36]. The shape optimization for the frequency related problem is an important part of the structure optimization [41]. By applying the shape optimization, the beam can achieve the maximum resonant frequencies in the bending and torsion modes [42]. And the algorithms for the shape optimization of the beam vibration problem are under development to improve the efficiency and robustness [43,44].

In this study, an analytical expression of the sensitivity is obtained for the mass resonator with a variable thickness. An algorithm is given for the resonant frequencies of the beam with an arbitrary thickness distribution. The sensitivity is validated by the finite element method (FEM) for the uniform and non-uniform beams. The cantilever and doubly clamped beams are the two most important types of beam for the resonators. The much larger sensitivities of the optimized beam shapes are achieved as compared with those of uniform ones. The effects of the minimum thickness and the axial stress in the optimization on the shapes and sensitivity are studied. This optimization method can be of significant help to the improvement on the sensitivity of the beam resonator.

Model development

Figure 1 is a schematic diagram of a beam resonator with thickness variation along the longitudinal direction (x-axis). The beam length and width are denoted as l and b, respectively. Based on the Euler-Bernoulli beam theory, the governing equation of the beam with a particle attached is as follows [34]:

$$\frac{\partial^2}{\partial x^2}\left[D(x)\frac{\partial^2 w(x,t)}{\partial x^2}\right]-T\frac{\partial^2 w(x,t)}{\partial x^2}+C\frac{\partial w(x,t)}{\partial t}+\left[\rho bh(x)+m\delta(x-x_p)\right]\frac{\partial^2 w(x,t)}{\partial t^2}=0, \tag{2}$$

where w is the transverse displacement of the beam neutral surface; t is time; $h(x)$ is the variable thickness along the x-axis; E and ρ are the Young's modulus and density of the beam, respectively; $D(x)=Ebh^3(x)/12$ is the bending stiffness of the beam; $\rho bh(x)$ is the beam mass per unit length varying with x; C is the viscous damping coefficient [45] and T is the axial load. The positive T is tension and the negative T is compression. Here $\delta(x\text{-}x_p)$ is the Dirac function and the effect of an adsorbed is

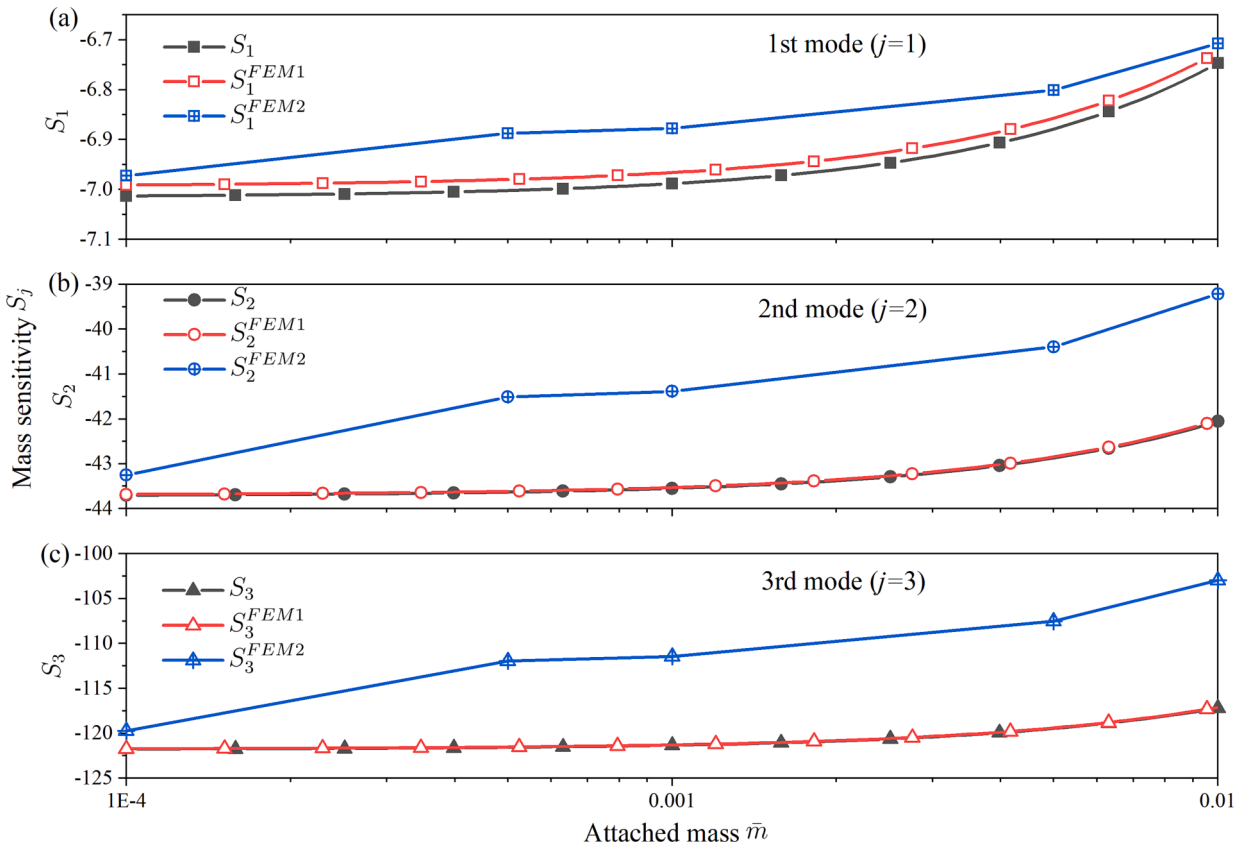

Fig. 3. Mass sensitivities, S_j, S_j^{FEM1} and S_j^{FEM2} of a uniform resonator from the present model with $N = 20$ and FEM, with different mode numbers: (a) $j = 1$; (b) $j = 2$; (c) $j = 3$.

modeled as a concentrated mass with the mass m and position x_p.

By using the derivations in Appendix A, the dimensionless sensitivity of the beam resonator with variable thickness is expressed as follows:

$$S_j = \frac{d\omega_j}{d\overline{m}} = -\left(1+\frac{1}{4Q_j^2}\right)\frac{\omega_j\phi_j^2(\xi_p)}{2\int_0^1 \overline{h}(\xi)\phi_j^2(\xi)\,\mathrm{d}\xi + \overline{m}\phi_j^2(\xi_p)}, \tag{3}$$

where Q_j is the quality factor of the j-th mode; ω_j and $\phi_j(\xi)$ are the dimensionless resonant frequency and mode shape, respectively; $\overline{h}$ and $\overline{m}$ are the dimensionless thickness and attached mass, respectively. Here ξ is the dimensionless quantity with $\xi = x/l$.

An implicit assumption in Eq. (3) is the small attached mass, which has no impact on the mode shape $\phi_j(\xi)$ of the resonator and thus ensure the accuracy of Eq. (A9). An adsorption increases the mass and as a result decreases the eigenfrequency. Therefore, the sensitivity in Eq. (3) is negative. Clearly, it is shown in Eq. (3) that the absolute value of sensitivity S_j decreases with the increase of the attached mass $\overline{m}$. Based on the study [34], the damping effect decreases the absolute value of the sensitivity. Because the resonant frequency ω_j decreases with the increase of the damping coefficient. Besides, the damping does not affect the mode shapes of resonators. Thus, by letting $\overline{m} = 0$ [46], neglecting the damping, i.e., $C = 0$ (or $Q\to\infty$) and taking the absolute value, the limit sensitivity S_j^l is expressed as follows:

$$S_j^l = \frac{\omega_j\phi_j^2(\xi_p)}{2\int_0^1 \overline{h}(\xi)\phi_j^2(\xi)d\xi}. \tag{4}$$

The limit sensitivity S_j^l is the maximum absolute value of the sensitivity S_j, reflecting the performance upper bound of the resonator. Equation (4) is the formula to compute the sensitivity of a beam resonator. Once the resonant frequency and mode shape are obtained, the limit sensitivity S_j^l can be calculated without solving Eq. (2). As to the uniform resonator, the expression of sensitivity can be reduced to the dimensionless format of Eq. (1), which is $S_j \approx -\frac{\omega_j\phi_j^2(\xi_p)}{2\int_0^1\phi_j^2(\xi)\mathrm{d}\xi}$ (as $\overline{h}\equiv 1$)..

The next step is to find the optimal beam shape $\overline{h}(\xi)$ for the maximum sensitivity. This gives the optimization problem to minimize the negative sensitivity S_j, which is expressed as follows:

$$\begin{cases} \text{minimize } S_j,\ j = 1,\ 2,\ 3\cdots, \\ a\leqslant\overline{h}(\xi)\leqslant b,\ \int_0^1 \overline{h}(\xi)\mathrm{d}\xi = H. \end{cases} \tag{5}$$

The constraint condition of $\int_0^1 \overline{h}(\xi)\mathrm{d}\xi = H$ restricts the volume of the resonator [47]: For a uniform beam, the only one possible situation is $\overline{h}(\xi) = H$. The constraint of $a\leqslant\overline{h}(\xi)\leqslant b$ controls the maximum and minimum thickness of the beam. These constraints provide the existence basis of the solution to the frequency related optimization problem [48]. As given in Eq. (4), the negative limit sensitivity, i.e., $-S_j^l$, is the minimum with neglecting the added mass and damping effect, which is the target function in this optimization problem. By dividing the beam length into N segments, the problem is solved with the interior point algorithm for the constrained nonlinear optimization problem [49]. The solution for the resonant frequency ω_j and mode shapes $\phi_j(\xi)$ is provided in Appendix B. The flowchart of the optimization procedures is presented in Fig. 2.

Results and discussion

Sensitivity validation

In this study, the beam material is silicon with the Young's modulus

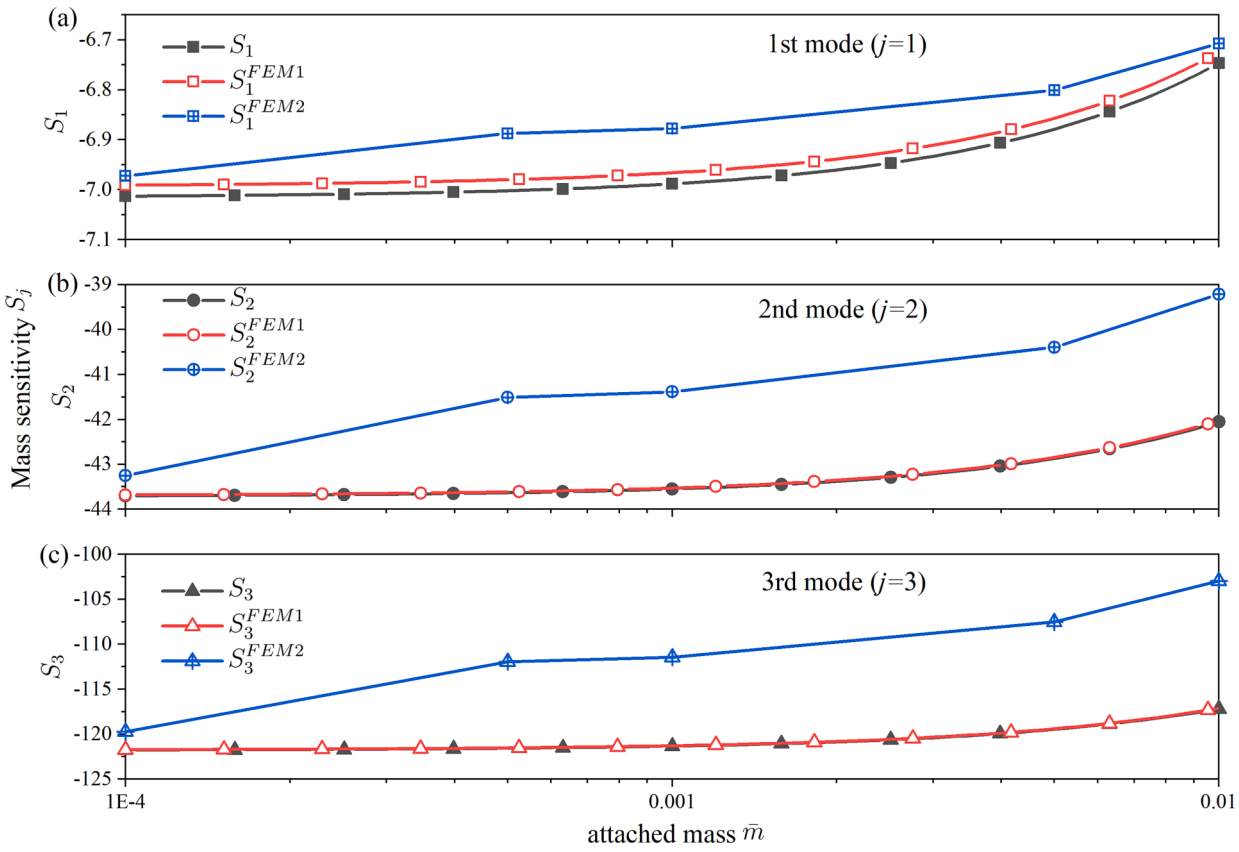

Fig. 4. Mass sensitivities, S_j, S_j^{FEM1} and S_j^{FEM2} of a tapered resonator from the present model with $N = 20$ and FEM, with different mode numbers: (a) $j = 1$; (b) $j = 2$; (c) $j = 3$.

of $E = 169$ GPa and mass density of $\rho = 2330$ kg/m^3; the beam length is $l = 500$ μm, the width is $b = 50$ μm and the reference thickness is $h_0 = 10$ μm [34].

In order to verify the sensitivity calculation of the present model, the vibration of the uniform cantilever with $\bar{h}(\xi) = 1$ and neglecting damping is studied, whose result is S_j as shown in Fig. 3. The two cases are also computed by FEM as the verification purpose, with the sensitivity results denoted as S_j^{FEM1} and S_j^{FEM2}, where j is the mode number. The two FEM sensitivity results are denoted as S_j^{FEM1} and S_j^{FEM2} in Fig. 3. Here S_j^{FEM1} is calculated from Eq. (3), where the resonant frequencies ω_j and mode shapes ϕ_j are computed from FEM model. S_j^{FEM2} is obtained from the definition $S_j^{\mathrm{FEM2}} = (\omega_{j,m} - \omega_{j,0})/\overline{m}$, where $\omega_{j,m}$ and $\omega_{j,0}$ are the resonant frequencies with and without the attached mass. In this case the particle is assumed to attach on the free end, i.e., $\xi_p = 1$. With the increase of the attached mass $\overline{m}$, the absolute values of the sensitivities decrease. As shown in Fig. 3, the FEM results S_j^{FEM2} are close to S_j of the present model. However, the differences between the numerical results S_j^{FEM2} and the present results S_j are becomes larger with the increase of the attached mass. When the attached mass is small, such as $\overline{m} = 10^{-4}$, the results of S_j approach to S_j^{FEM2}, which validates the present model for predicting the sensitivity for the beams with a small particle attached. The main reasons for the difference are the approximation of using the Dirac function $\delta(\xi\text{-}\xi_p)$ to describe the particle attachment, and the assumption of that particle attachment will not change the mode shape of the beam vibration.

For the tapered cantilever, whose thickness is defined as $\bar{h}(\xi) = 1.5 - \xi$, the mass sensitivity results of S_j, S_j^{FEM1} and S_j^{FEM2} are shown in Fig. 4. In this case, the segment number N is set as 20. Shown in the figure, the differences between the three prediction results are smaller when the attached mass is less. The relative differences of S_j and S_j^{FEM2} ($j = 1, 2, 3$) are only about 0.6%, 1.4% and 2.2%, respectively. The sensitivity results of the doubly clamped non-uniform beam are presented in Fig. 5, whose thickness is expressed as $\bar{h}(\xi) = 0.5 + |1 - 2\xi|$. The relative differences of S_j and S_j^{FEM2} ($j = 1, 2, 3$) are about 0.5%, 4.1% and 6.0%, respectively. Therefore, the present sensitivity prediction method of Eq. (3) is more effective and easier than FEM for the small particle situation.

Sensitivity optimization of the beam resonators

The largest sensitivities for the cantilevers are the situations when the attached particles are located at the free end, as reflected in Eq. (4). Based on this, the optimization results of the cantilevers are shown in Fig. 6(a) and (b). In this case, the constraint parameters for the optimization are $a = 0.02$, $b = 2$ and $H = 1$. The segment number $N = 20$. The particles position of the $j = 1$ and 2 cases is $\xi_p = 1$, for the resonator can reach the maximum sensitivity when the displacement of the mode shape at the particle position is the largest. When mode numbers j are different, the optimized shapes are different with each other, whose limit sensitivities are: $S_1^l = 7.64 \times 10^3$ and $S_2^l = 2.85 \times 10^4$. The computation shows the specific shape of the resonators can enormously improve the frequency sensitivity on the attached mass. Compared with the uniform beam, whose sensitivity S_1^l is only 7.0, the improvement is astonishingly 1090 times.

As to the doubly clamped beams, the system can achieve the largest sensitivity when the particle is located at the beam center for $j = 1$ and 3, which is $\xi_p = 0.5$. Usually, the symmetrical modes are considered in the vibration excitation and analysis of the doubly clamped resonators with the particle attached at middle center [50,51]. Therefore, the second mode is not considered for the doubly clamped resonators. With the optimization parameter of $a = 0.02$, $b = 2$, $H = 1$ and $N = 40$, the results

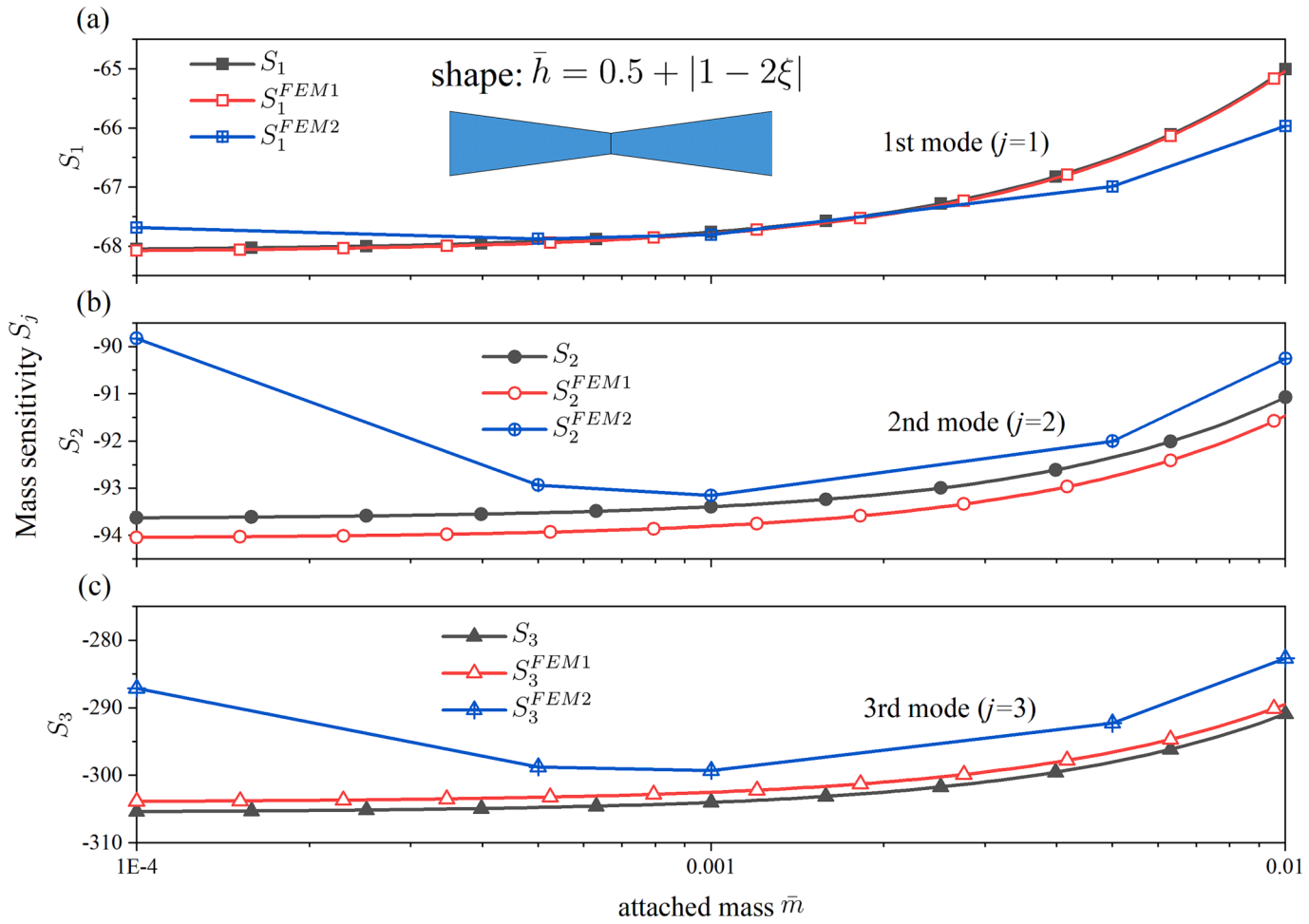

Fig. 5. Mass sensitivities, S_j, S_j^{FEM1} and S_j^{FEM2} of a doubly-clamped non-uniform resonator from the present model with $N = 20$ and FEM, with different mode numbers: (a) $j = 1$; (b) $j = 2$; (c) $j = 3$.

are shown in Fig. 7. The sensitivities are $S_1^l = 2.42 \times 10^4$ and $S_3^l = 7.47 \times 10^4$, much larger than $S_1^l = 28.2$ and $S_3^l = 119.5$ of the uniform beam. The optimized shapes of the beam are curve-fitted in Appendix D.

The mode shapes of the uniform and optimized cantilever and doubly clamped beams are shown in Fig. 8. As seen in Fig. 8(a) for the cantilever beam, there is hardly any displacement when $\xi < 0.9$ in the mode shape of the optimized beam. But an abrupt displacement increase is around the free end. This abrupt displacement increase is the key to the sensitivity improvement of an optimized cantilever beam. As seen in Eq. (4), the mode shapes of the optimized beams are to reduce the value of $\int_0^1 \bar{h}(\xi)\phi_j(\xi)\phi_j(\xi)\mathrm{d}\xi$. On the other hand, the kinetic energy of the vibration is heavily concentrated around the free end. It is assumed that the maximum kinetic energy and maximum strain energy of the resonator are both same before and after the particle attachment [19]. The particle locates at position with larger displacement will affects the resonant frequency more. This leads to the high sensitivity of this optimized resonator. Thus the antinode, which is largest displacement of a mode, is the largest sensitivity location of the resonator. In addition, the inertias of the optimized beams are much lower than those of the uniform beams, which improves the resonant frequencies and the sensitivities. Similarly, the "energy trapping" is found in the thicker electrodes [52], which can be used to adjust the sensors' performance.

For the vibration of the axially inhomogeneous beams, the jump phenomenon of the natural frequency happens with the axial gradient increase of the stiffness [53,54]. The reason is the propagating wave cannot be excited when the frequency is less than the critical frequency of the axially inhomogeneous beams and thus the harmonic vibration of the beam is impossible [53,54]. There may be more than one nodes in the first mode shape of the axially inhomogeneous beams [53,54]. This phenomenon may also happen for the beam with variable thickness. However, in this study, as an example of the cantilever, the stiffness is decreasing from the clamped end to the free end. In the closer looks of mode shapes, the node numbers are separately 0, 1 and 2 for the mode number $j = 1$, 2 and 3, which can be seen in Fig. 8(c) and (d).

To verify the convergence of the optimization results, different segment numbers N and initial guesses are tested in the optimization process. Figure 9 shows the optimization results for cantilevers and the segment numbers are $N = 20$, 35 and 50, respectively. The beam shapes are close with different segment numbers N. With the increasing N, the optimized shapes are consistent. $N = 20$ is enough to obtain the optimal shapes of the resonators. Figure 10(a) shows the different initial guesses of the beam shapes in the shape optimization. Figure 10(b) displays the optimization results of these different initial guesses. The results are exactly the same.

The sensitivity of resonator is dependent on the particle locations, which is seen from Eq. (4). The frequency keeps unchanged when the particle is located at the node of the mode shapes [55]. The optimized beam shape gives a larger sensitivity than the uniform one at $\xi_p = 1$. However, it is hard to control the particle position precisely in the measuring process [56]. Figure 11 shows the limit sensitivities S_j^l of the optimized and uniform beam shapes with different particle locations ξ_p. When the particle is close to the free end, the sensitivity of the optimized shape is much higher. For the cantilever results in Fig. 11(a), using the

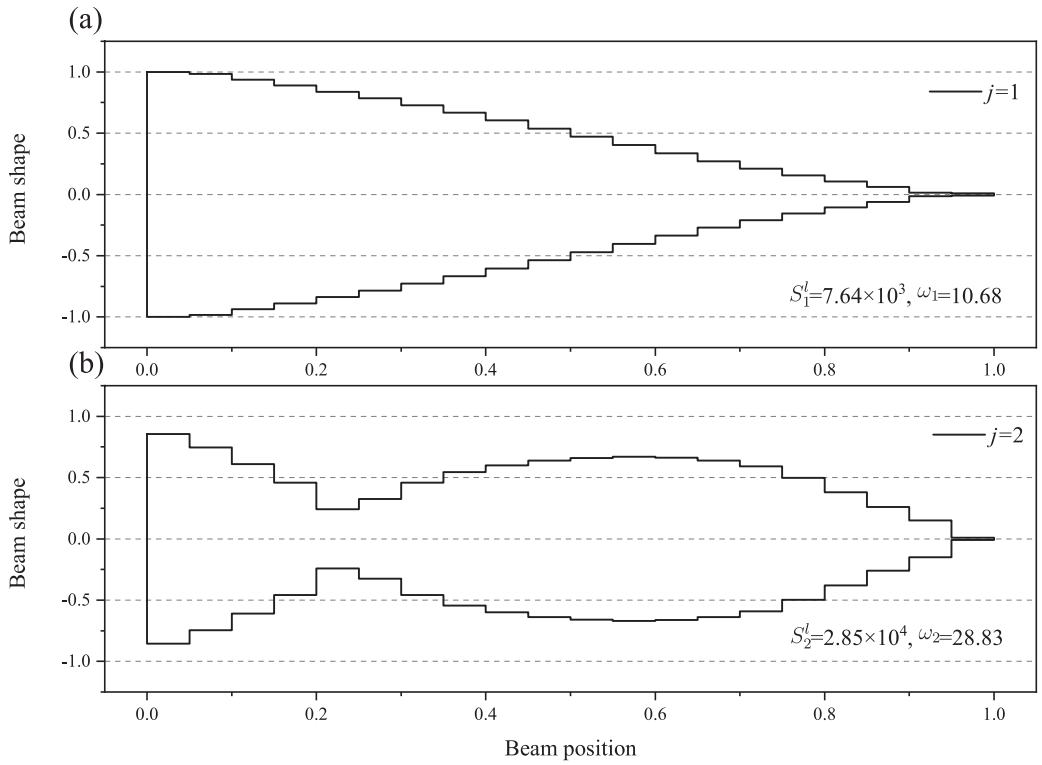

Fig. 6. Optimization results of the cantilevered beam for $j = 1$ and 2: (a) Optimized beam shape for $j = 1$; (b) Optimized beam shape for $j = 2$.

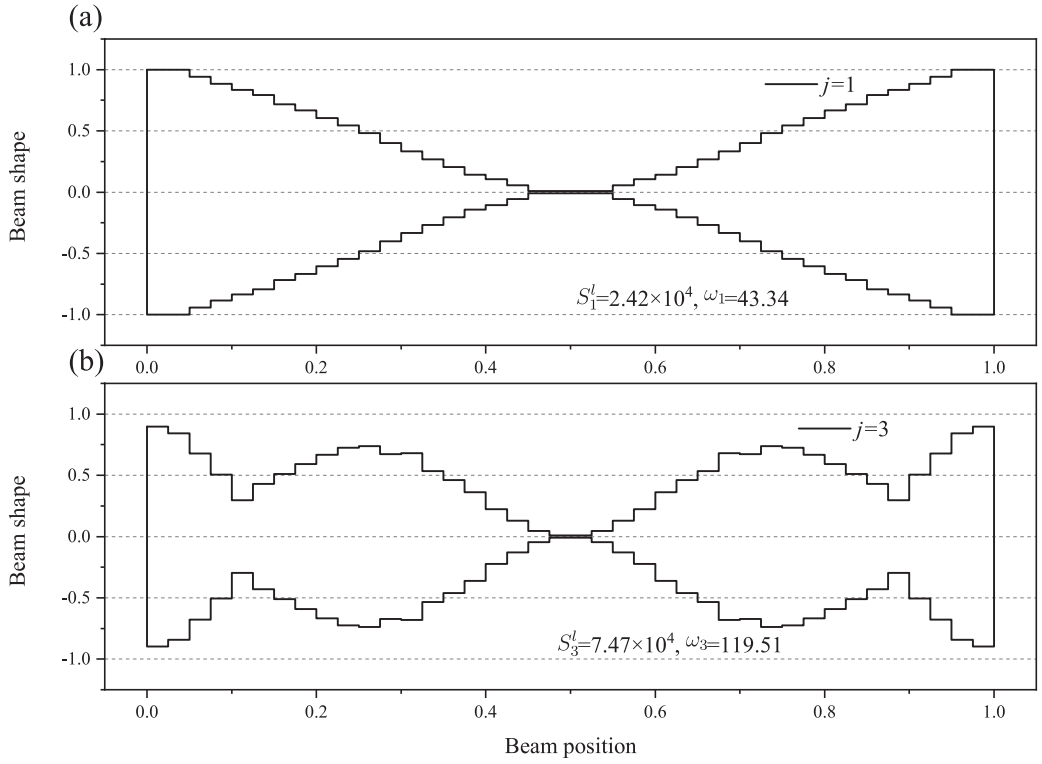

Fig. 7. Optimization results of the doubly-clamped beam for $j = 1$ and 3: (a) Optimized beam shape for $j = 1$; (b) Optimized beam shape for $j = 3$.

optimized shape needs the particle to locates at the range [0.7, 1], to achieve a better sensitivity than the uniform one. However, for the second mode in Fig. 11(b), only when $\xi_p > 0.97$ can the sensitivity of the optimized shape be better. For the doubly clamped beams, the particle location should be in [0.4, 0.6] for $j = 1$ and [0.45, 0.55] for $j = 3$, to get a greater sensitivity. This implies the higher modes ($j > 2$) are not suitable for the shape optimization, for the particle location range is too narrow to be controlled. For the first mode, using the shape optimization is an effective method to improve the sensitivity in measurement.

The thickness ratio μ is defined as $\mu = a/H$. As mentioned above,

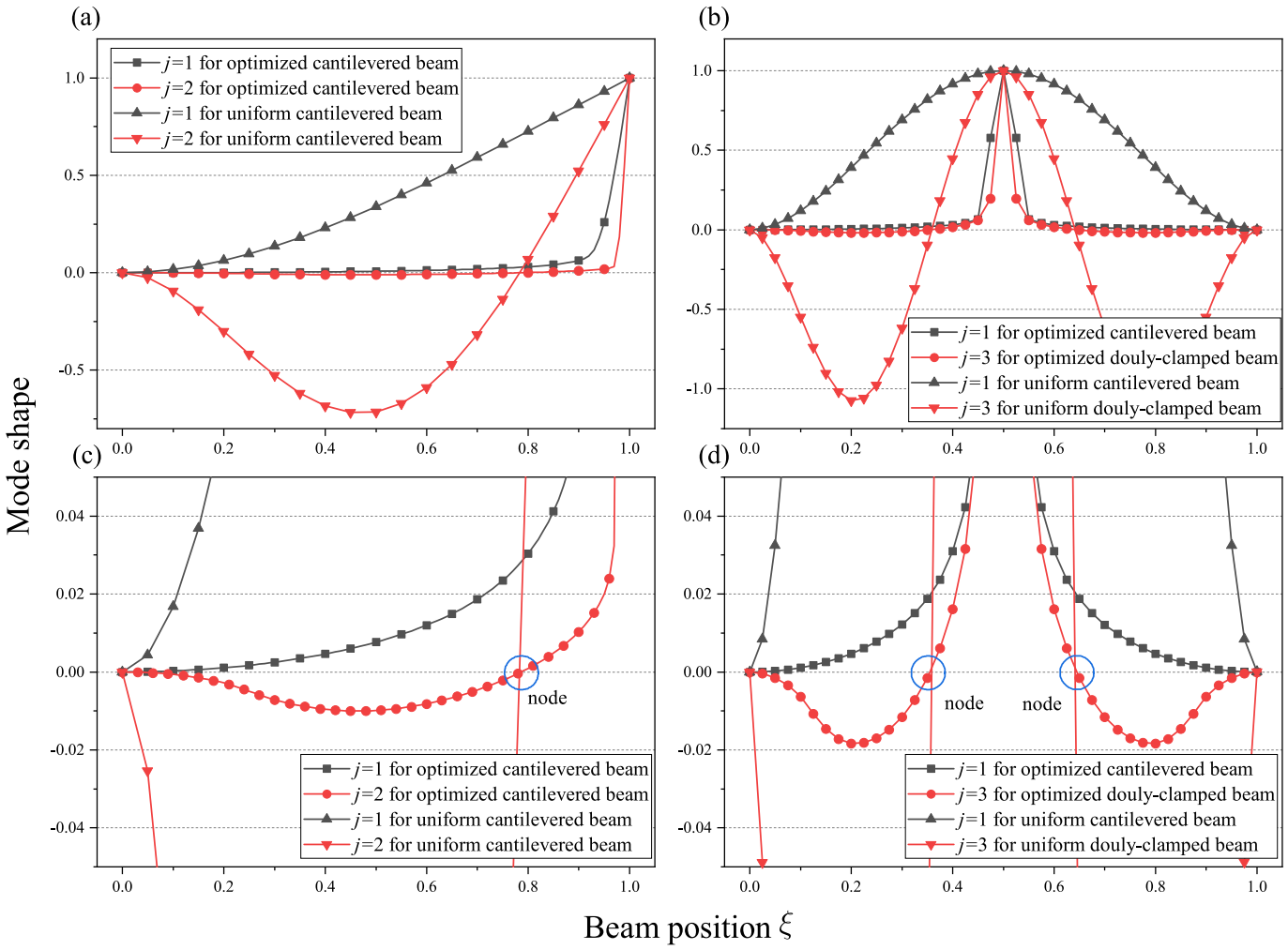

Fig. 8. Mode shapes of the optimized and uniform beams, (a) for cantilevered beam and (b) for doubly clamped beam. (c) and (d) are the closer looks of (a) and (b), respectively.

$a \leq \overline{h} \leq b$, a is the smallest beam thickness. The parameter μ determines the minimum thickness of the resonator, which is relevant with the actual fabrication ability of the micro/nano-resonators. To investigate this, the different μ values of $\mu = 0.02$, 0.05, 0.1, 0.5 and 1 are investigated in the optimization. The optimization results of the cantilevered and doubly clamped beams are presented in Fig. 12 and Fig. 13, respectively. The relations between the optimized beam shapes with different μ can be viewed as follows: First, the beam shape with $\mu = 0.02$ is the basic shape of the optimization; Then, the thickness at some position, which is less than the constraint μ, is replaced with the lower bound μ; At last, the beam shape result is normalized with the constraint $\int_0^1 \overline{h}(\xi)\mathrm{d}\xi = H$. This process implies that the basic shapes of the results are similar. However, their sensitivity results are very different, as in Fig. 12(c) and Fig. 13(b). The parameter μ has a great influence on the sensitivity results, which exceeds the influence of the higher mode. Similarly, the smaller substructure can improve the power generation of the piezoelectric energy harvesters [57].

The axial tension on the string resonator will improve the resonant frequencies and the sensitivity [30]. However it would not improve the sensitivity for the non-uniform resonator by applying the axial tension. By applying the shape optimization on the cantilevers and doubly clamped beams with mode number $j = 1$, the optimal results of the beam shapes, mode shapes, limit sensitivity and resonant frequencies are displayed in Fig. 14 and Fig. 15. With the variation of the axial load, only small changes in the optimized optimal shapes are shown in Fig. 14 (a) and Fig. 15 (a). However, from Fig. 14 (c) and Fig. 15 (c), the limit sensitivities are decreasing with the increase of the axial load, which is opposite to the uniform resonators. The major reason is that the mode shapes are stretched by the axial load, which induces the decrease of the integration $\int_0^1 \overline{h}(\xi)\phi_j(\xi)\phi_j(\xi)\mathrm{d}\xi$, shown in Fig. 14 (b). Although the resonant frequencies are increasing, the sensitivities are reduced with the increase of the axial tension. For the resonant frequencies will keep decreasing and finally become zero with adding on the negative (compressed) load, the sensitivity will become much lower with a large compression on the resonator. Thus, the conclusion is only suitable for the small and moderate load.

Conclusion

The shape optimization problem for the resonator with variable thickness is proposed and solved numerically to greatly improve the sensitivity. The sensitivity expression, which serves as the object function for optimization, is obtained by using the approximation method. As the optimization results, the beam shapes of maximum sensitivity are obtained for the cantilevered and doubly clamped beams, and the limit sensitivity of the resonators can be more than one thousand times higher than that of the uniform ones. Moreover, to use the shape optimization to improve the sensitivity demands for both the restricted particle attachment locations and low damping. Physically, to improve the sensitivity, it is expected for the resonator to concentrate the kinetic

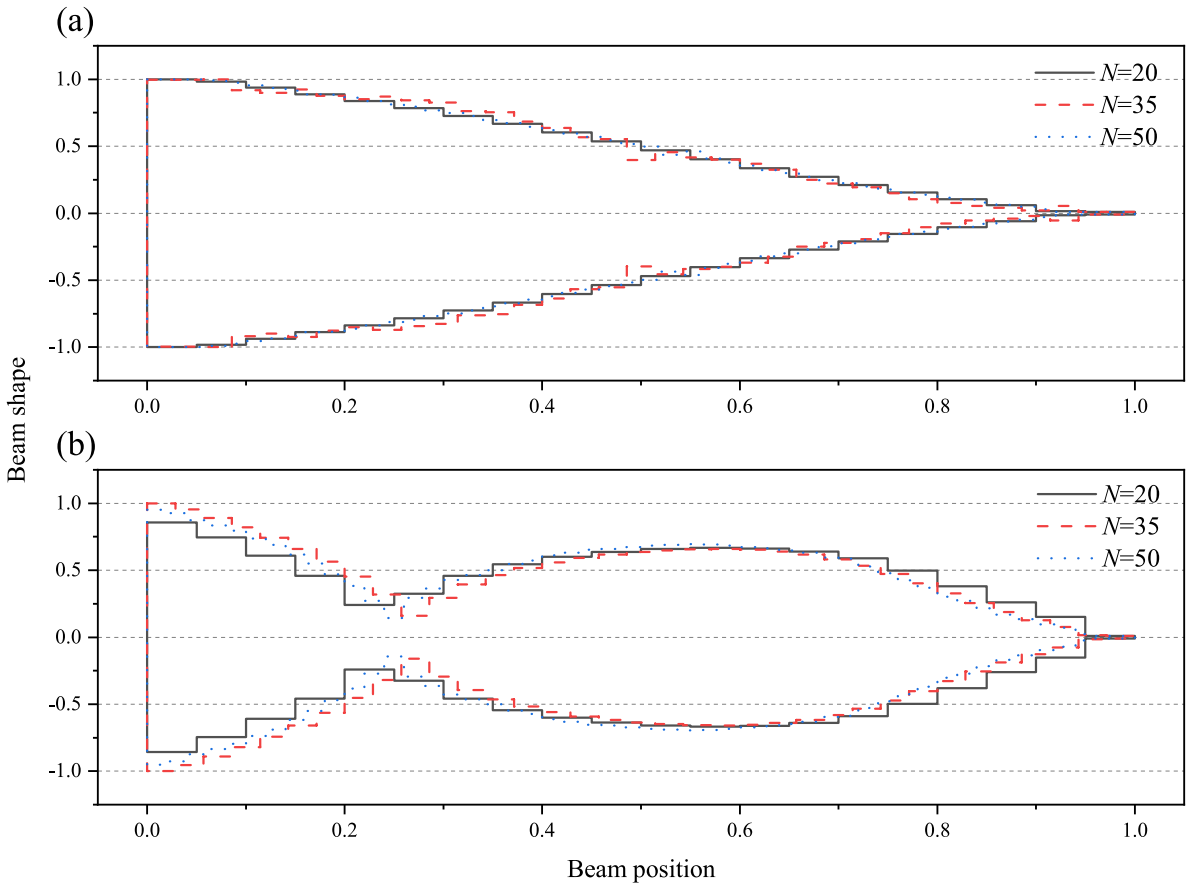

Fig. 9. Optimization results for the cantilevers with different segment numbers N, for (a) mode number $j = 1$ and (b) mode number $j = 2$.

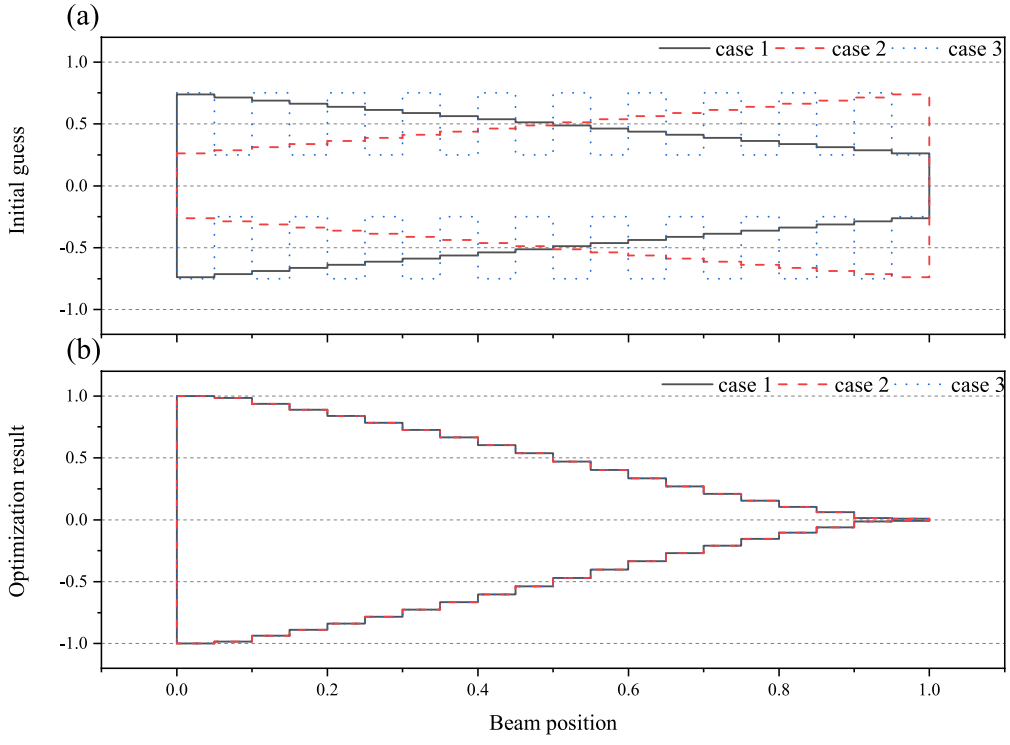

Fig. 10. (a) Different initial guesses on the beam thickness variation and (b) the optimization results of the different cases.

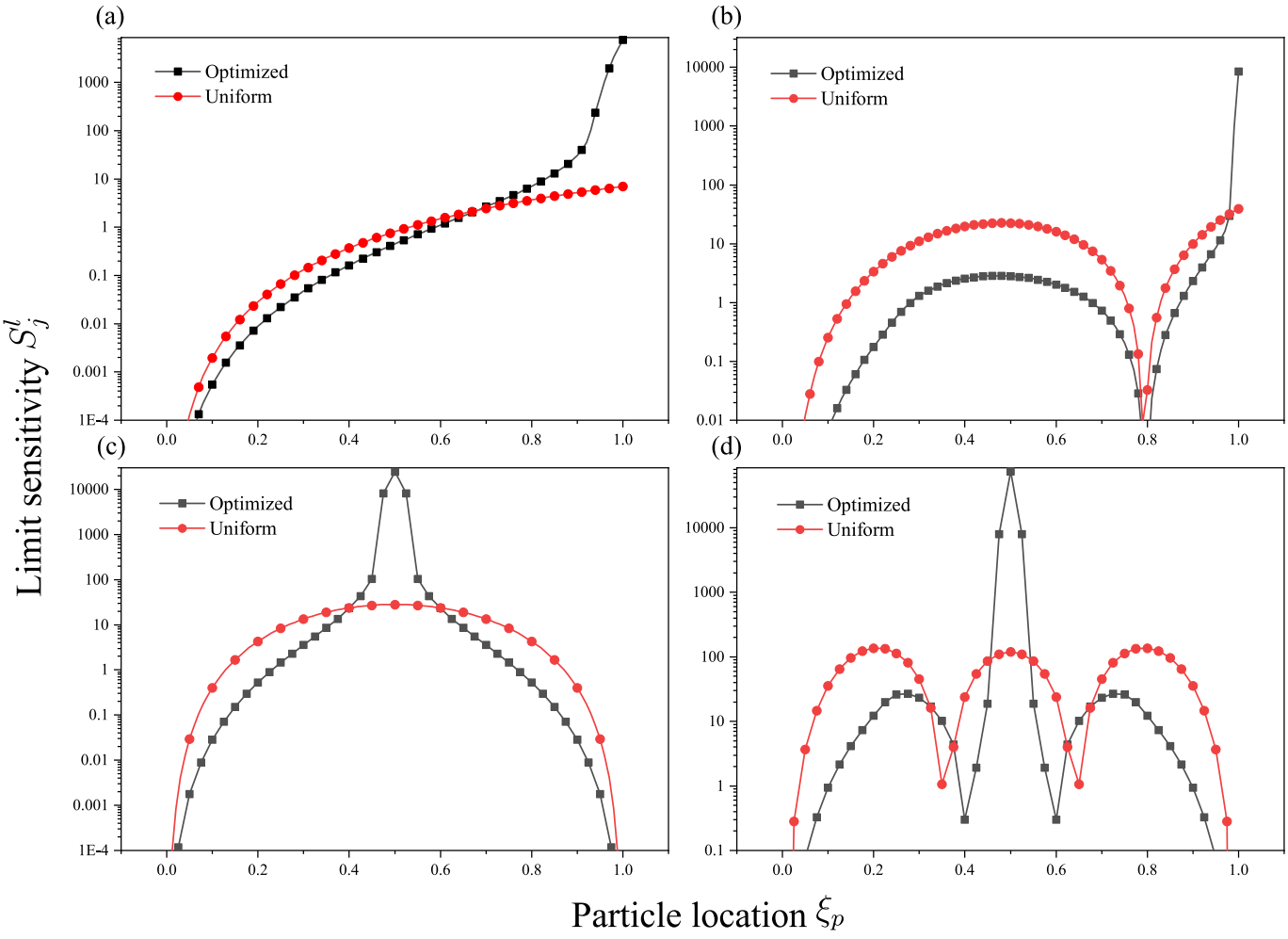

Fig. 11. The limit sensitivity of the optimized and uniform beam shapes with different particle locations. (a) for cantilevers and $j = 1$; (b) for cantilevers and $j = 2$; (c) for doubly clamped beams and $j = 1$; (d) for doubly clamped beams and $j = 3$.

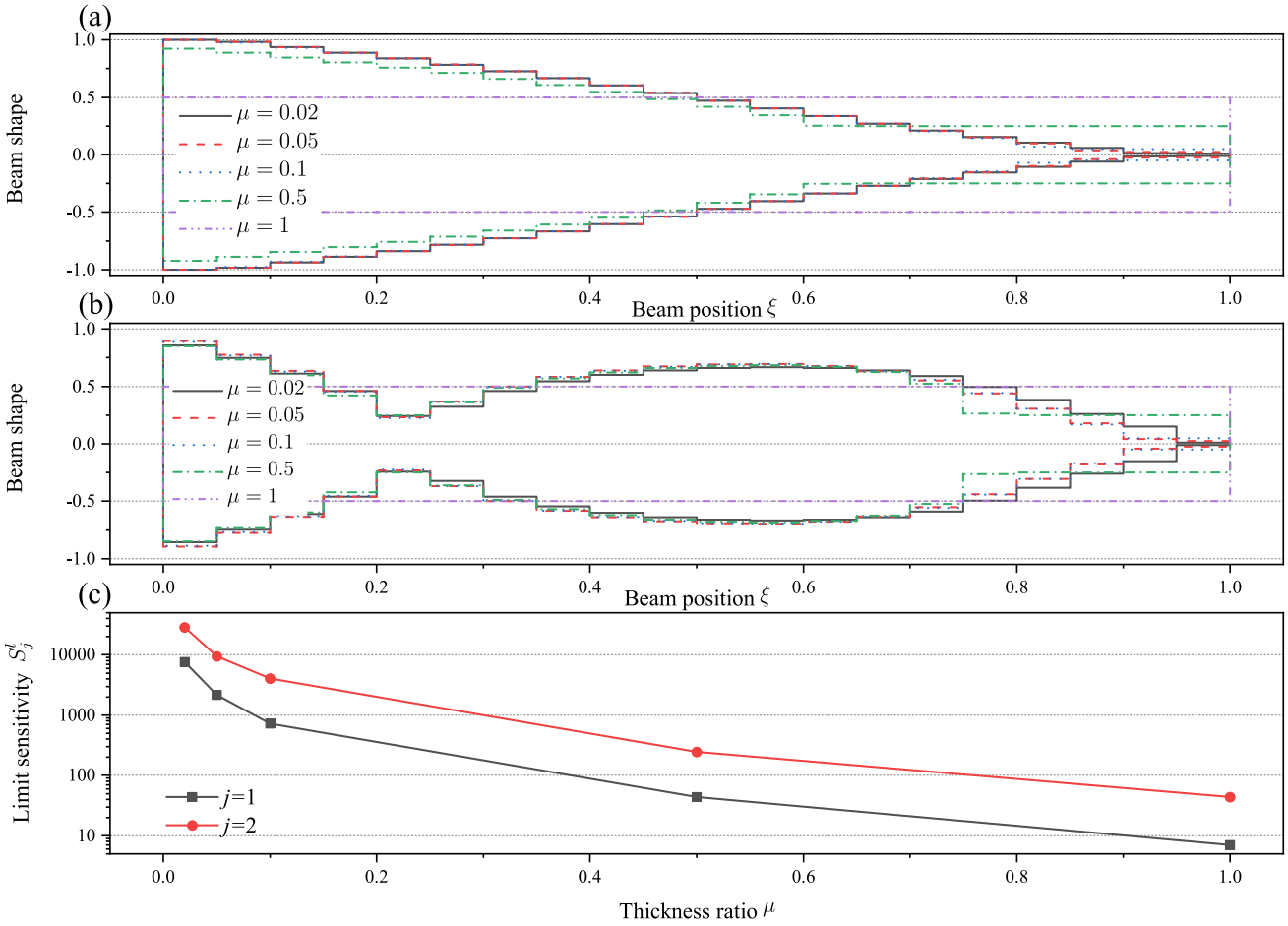

Fig. 12. The optimization results of the cantilevered beam with different thickness ratio μ for $j = 1$ and $j = 2$, respectively: (a) The mode shapes of the optimized beams with $j = 1$; (b) The mode shapes of the optimized beams with $j = 2$. The critical sensitivity results of the optimal beam outline for the different thickness ratio μ.

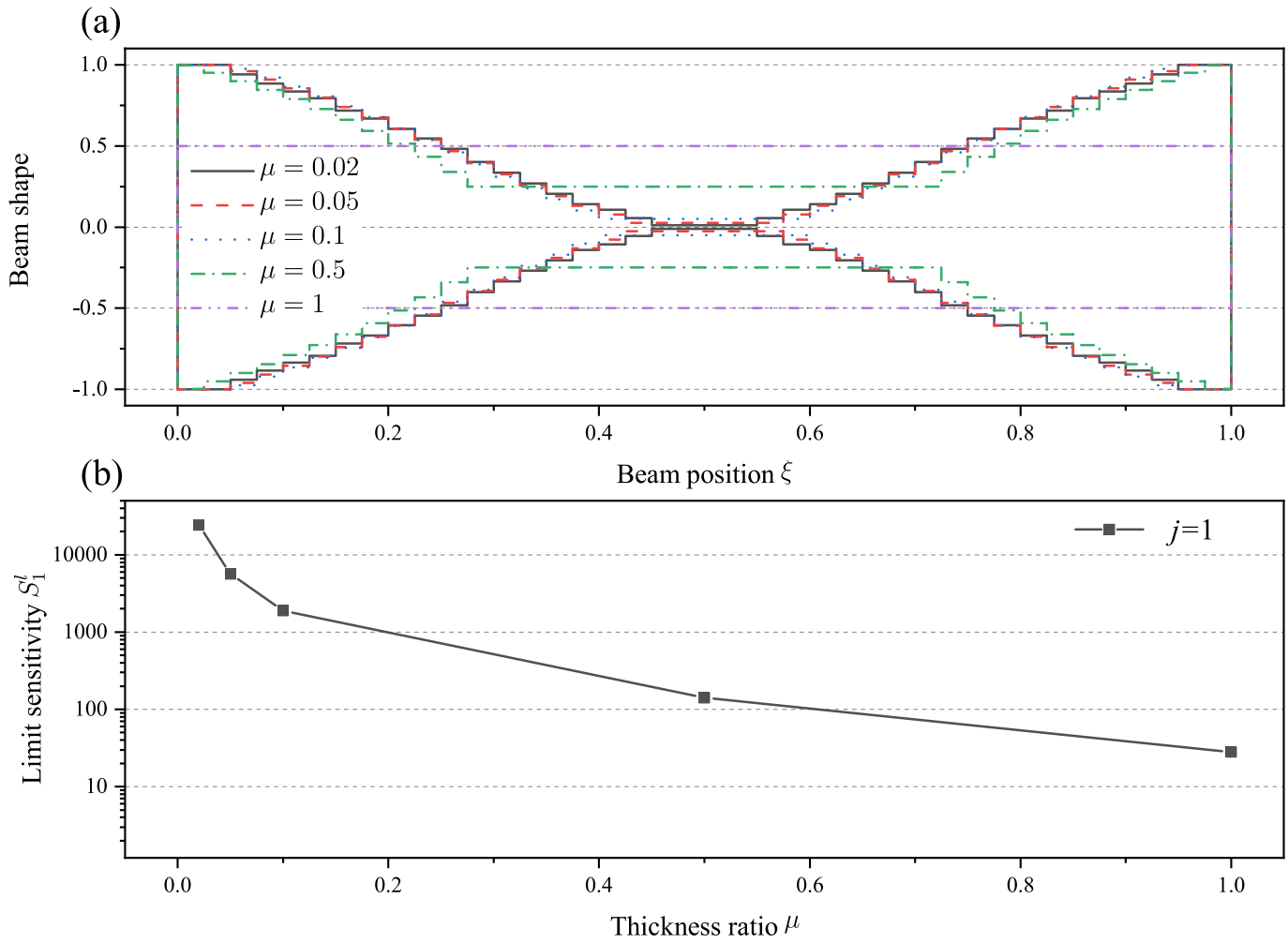

Fig. 13. The optimization results of the doubly clamped beam with different thickness ratio μ for $j = 1$: (a) The mode shapes of the optimized beams; (b) The critical sensitivity results of the optimal beam outline for the different thickness ratio μ.

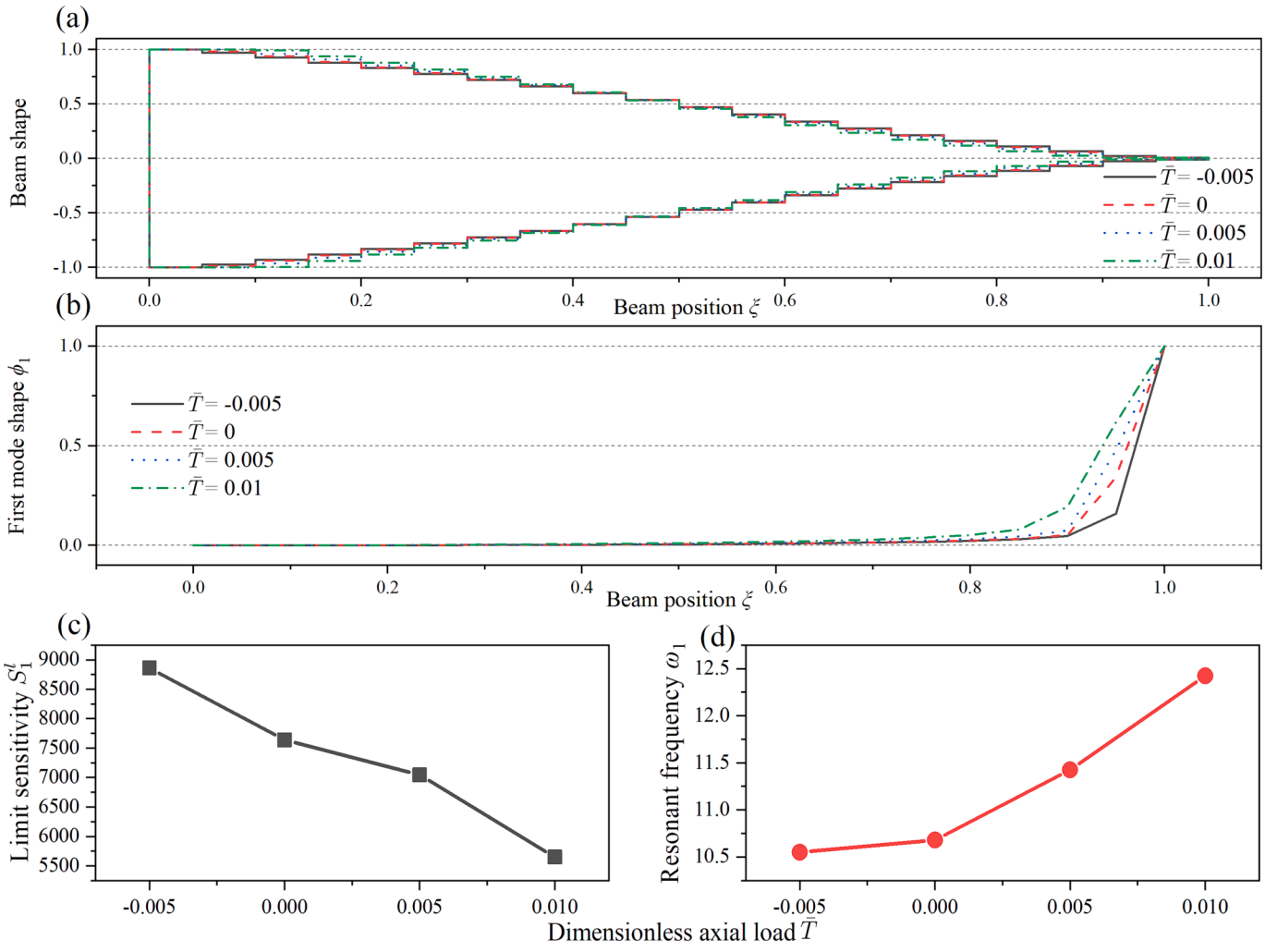

Fig. 14. The optimization results with the different axial load $\overline{T}$ of a cantilever: (a) The optimal beam shapes; (b) The first mode shapes; (c) The first limit sensitivities; (d) The first resonant frequencies.

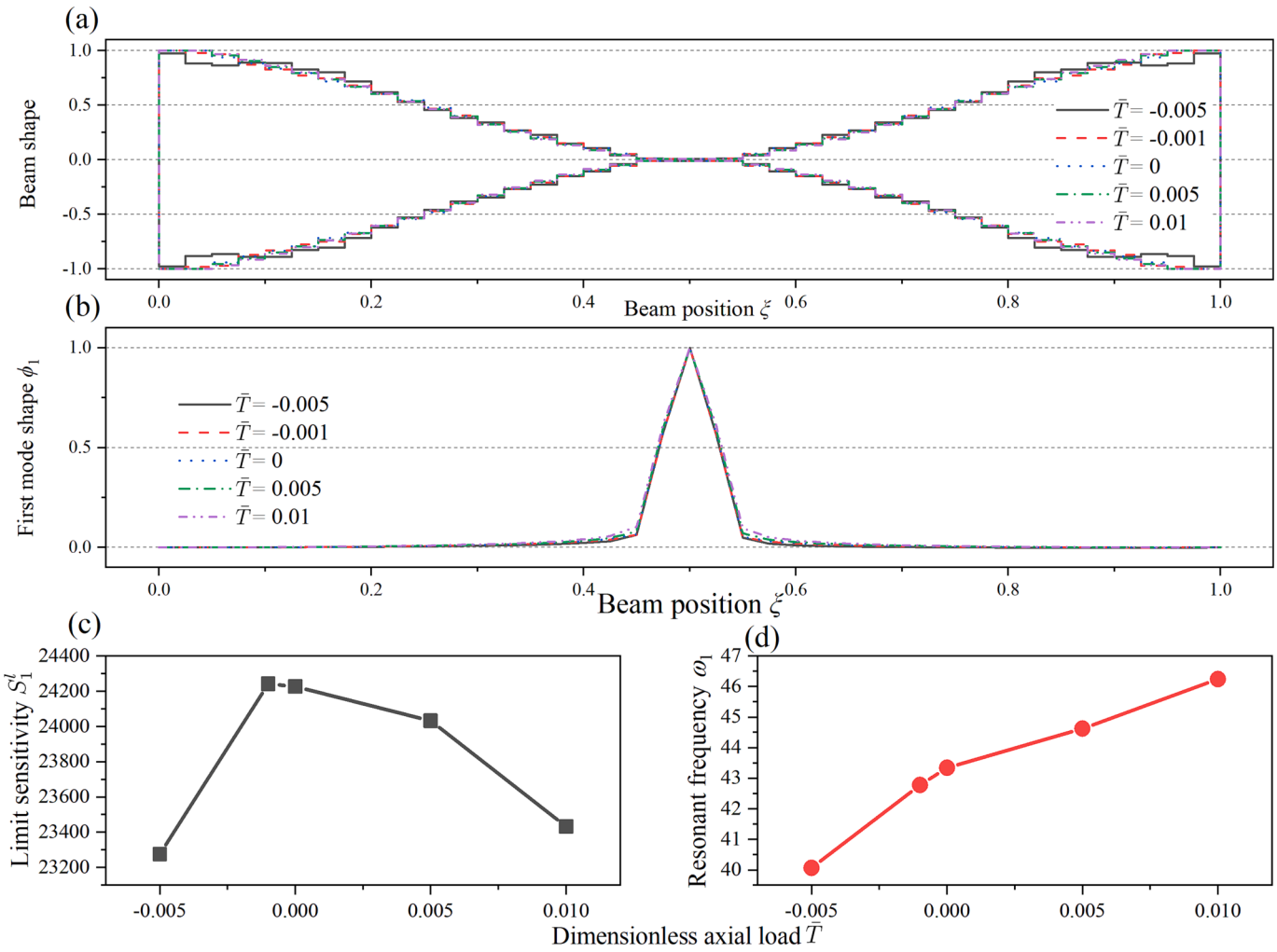

Fig. 15. The optimization results with the different axial load $\overline{T}$ of a doubly clamped beam: (a) The optimal beam shapes; (b) The first mode shapes; (c) The first limit sensitivities; (d) The first resonant frequencies.

energy on the antinode, at meanwhile, the attached particle also needs to stay at the antinode. Furthermore, the small axial compression also contributes to the sensitivity improvements for the resonators in our analysis.

CRediT authorship contribution statement

Chenxi Wei: Conceptualization, Investigation, Methodology, Software, Formal analysis, Writing – original draft. **Yin Zhang:** Conceptualization, Investigation, Methodology, Resources, Supervision, Writing – review & editing, Funding acquisition.

Declaration of Competing Interest

The authors declare that they have no known competing financial interests or personal relationships that could have appeared to influence the work reported in this paper.

Data availability

No data was used for the research described in the article.

Acknowledgments

This work was supported by the National Natural Science Foundation of China (NSFC No. 11772335) and the Ministry of Science and Technology of China (No. 2022YFE0124700).

Appendix A. Expression derivation of the sensitivity

The governing equation of the beam with a particle attached is as follows:

$$\frac{\partial^2}{\partial x^2}\left[D(x)\frac{\partial^2 w(x,t)}{\partial x^2}\right] - T\frac{\partial^2 w(x,t)}{\partial x^2} + C\frac{\partial w(x,t)}{\partial t} + \left[\rho bh(x) + m\delta(x-x_p)\right]\frac{\partial^2 w(x,t)}{\partial t^2} = 0, \tag{A1}$$

The boundary conditions of a cantilever beam are as follows:

$$w(0,t)=0,\frac{\partial w(0,t)}{\partial x}=0,\frac{\partial^2 w(l,t)}{\partial x^2}=0,\frac{\partial}{\partial x}\left[D(l)\frac{\partial^2 w(l,t)}{\partial x^2}\right]-T\frac{\partial w(l,t)}{\partial x}=0. \tag{A2}$$

The boundary conditions of a doubly clamped beam are as follows:

$$w(0,t)=0,\frac{\partial w(0,t)}{\partial x}=0,w(l,t)=0,\frac{\partial w(l,t)}{\partial x}=0. \tag{A3}$$

By introducing the quantities of $\xi=x/l,\ \tau=t\sqrt{Eh_0^2/12\rho l^4}$ and $W=w/l$, the governing equation of Eq. (A1) is now non-dimensionalized as follows:

$$\frac{\partial^2}{\partial\xi^2}\left[\overline{D}(\xi)\frac{\partial^2 W(\xi,\tau)}{\partial\xi^2}\right]-\overline{T}\frac{\partial^2 W(\xi,\tau)}{\partial\xi^2}+\overline{C}\frac{\partial W(\xi,\tau)}{\partial\tau}+\left[\overline{h}(\xi)+\overline{m}\delta(\xi-\xi_p)\right]\frac{\partial^2 W(\xi,\tau)}{\partial\tau^2}=0, \tag{A4}$$

where the dimensionless quantities and functions are defined as the following:

$$\overline{h}(\xi)=\frac{h(\xi)}{h_0},\overline{D}(\xi)=\overline{h}^3(\xi),\overline{T}=\frac{12Tl^2}{Ebh_0^3},\overline{C}=C\sqrt{\frac{12l^4}{E\rho bh_0^4}},\overline{m}=\frac{m}{\rho bh_0 l},\xi_p=\frac{x_p}{l}. \tag{A5}$$

Here h_0 is a reference quantity to measure the thickness of the beam, which can be arbitrary. But it is recommended to define $h_0=\frac{1}{l}\int_0^l h(x)\mathrm{d}x$, which is the average thickness over the length.

The dimensionless boundary conditions of a cantilever and a doubly clamped beams now become the following:

$$W(0,\tau)=0,\frac{\partial W(0,\tau)}{\partial\xi}=0,\frac{\partial^2 W(1,\tau)}{\partial\xi^2}=0,\frac{\partial}{\partial\xi}\left[\overline{D}(1)\frac{\partial^2 W(1,\tau)}{\partial\xi^2}\right]-\overline{T}\frac{\partial W(1,\tau)}{\partial\xi}=0. \tag{A6}$$

and

$$W(0,\tau)=0,\frac{\partial W(0,\tau)}{\partial\xi}=0,W(1,\tau)=0,\frac{\partial W(1,\tau)}{\partial\xi}=0. \tag{A7}$$

For the j-th order resonance, the solution is assumed to be $W(\xi,\tau)=\phi_j(\xi)\mathrm{e}^{(i\omega_j-\gamma_j)\tau}$, where $\phi_j(\xi)$ is the j-th mode shape, ω_j is the dimensionless j-th eigenfrequency and γ_j is the dimensionless j-th decay rate of the system. By using approximation method [58], the following equation is obtained:

$$\begin{cases}\omega_j^2-\gamma_j^2=\dfrac{\displaystyle\int_0^1\left\{\frac{\partial^2}{\partial\xi^2}\left[\overline{D}(x)\frac{\partial^2\phi_j(\xi)}{\partial\xi^2}\right]-\overline{T}\frac{\partial^2\phi_j(\xi)}{\partial\xi^2}-\gamma_j\overline{C}\phi_j(\xi)\right\}\phi_j(\xi)\mathrm{d}\xi}{\displaystyle\int_0^1\left[\overline{h}(\xi)+\overline{m}\delta(\xi-\xi_p)\right]\phi_j^2(\xi)\,\mathrm{d}\xi},\\ \gamma_j=\dfrac{\overline{C}}{2}\dfrac{\displaystyle\int_0^1\phi_j^2(\xi)\,\mathrm{d}\xi}{\displaystyle\int_0^1\left[\overline{h}(\xi)+\overline{m}\delta(\xi-\xi_p)\right]\phi_j^2(\xi)\,\mathrm{d}\xi}.\end{cases} \tag{A8}$$

In conjunction with the Dirac delta function property, Eq. (A8) leads to the following results:

$$\begin{cases}\omega_j=\sqrt{\dfrac{\displaystyle\int_0^1\left\{\frac{\partial^2}{\partial\xi^2}\left[\overline{D}(x)\frac{\partial^2\phi_j(\xi)}{\partial\xi^2}\right]-\overline{T}\frac{\partial^2\phi_j(\xi)}{\partial\xi^2}-\gamma_j\overline{C}\phi_j(\xi)\right\}\phi_j(\xi)\,\mathrm{d}\xi}{\displaystyle\int_0^1\overline{h}(\xi)\phi_j^2(\xi)\,\mathrm{d}\xi+\overline{m}\phi_j^2(\xi_p)}+\gamma_j^2},\\ \gamma_j=\dfrac{\overline{C}}{2}\dfrac{\displaystyle\int_0^1\phi_j^2(\xi)\,\mathrm{d}\xi}{\displaystyle\int_0^1\overline{h}(\xi)\phi_j^2(\xi)\,\mathrm{d}\xi+\overline{m}\phi_j^2(\xi_p)}.\end{cases} \tag{A9}$$

The dimensionless sensitivity S_j is defined as the ratio of the dimensionless resonant frequency shift to the dimensionless attached mass $\overline{m}$ [17,19]. The sensitivity reflects the resonator capability to detect the ultra-small particles, which is

$$S_j=\frac{\mathrm{d}\omega_j}{\mathrm{d}\overline{m}}=-\left(\omega_j+\frac{\gamma_j^2}{\omega_j}\right)\frac{\phi_j^2(\xi_p)}{2\int_0^1\overline{h}(\xi)\phi_j^2(\xi)\,\mathrm{d}\xi+\overline{m}\phi_j^2(\xi_p)}. \tag{A10}$$

Alternatively, Eq. (A10) can be rewritten as follows:

$$S_j=\frac{d\omega_j}{d\overline{m}}=-\left(1+\frac{1}{4Q_j^2}\right)\frac{\omega_j\phi_j^2(\xi_p)}{2\int_0^1\overline{h}(\xi)\phi_j^2(\xi)\,\mathrm{d}\xi+\overline{m}\phi_j^2(\xi_p)}, \tag{A11}$$

where Q_j is the quality factor of the j-th mode.

Appendix B. Numerical solution for the beam vibration with variable thickness

Now we introduce a numerical method to solve the vibration of a beam in variable thickness, whose governing equation is given as follows:

$$\frac{\partial^2}{\partial\xi^2}\left[\overline{D}(\xi)\frac{\partial^2 W(\xi,\tau)}{\partial\xi^2}\right]-\overline{T}\frac{\partial^2 W(\xi,\tau)}{\partial\xi^2}+\overline{h}(\xi)\frac{\partial^2 W(\xi,\tau)}{\partial\tau^2}=0. \tag{B1}$$

The operator of Eq. (B1) is proved to be self-adjoint in Appendix C, which gives the real eigenvalue of the system [59].

The steady-state solution of the dimensionless transverse displacement is assumed to be $W(\xi,\ \tau)\ =\ Y(\xi)\cdot e^{i\omega\tau}$, in which $Y(\xi)$ is the spatial displacement part of the solution and $e^{i\omega\tau}$ is the temporal one. When the beam is at the j-th resonance, $Y(\xi) = c_j\phi_j(\xi)$. By substituting $W(\xi,\ \tau) = Y(\xi)\cdot e^{i\omega\tau}$ into Eq. (B1), the ordinary differential equation is obtained:

$$\frac{\mathrm{d}^2}{\mathrm{d}\xi^2}\left[\overline{D}(\xi)\frac{\mathrm{d}^2 Y(\xi)}{\mathrm{d}\xi^2}\right]-\overline{T}\frac{\mathrm{d}^2 Y(\xi)}{\mathrm{d}\xi^2}=\omega^2\overline{h}(\xi)Y(\xi). \tag{B2}$$

By defining the state vector $\boldsymbol{\theta}(\xi)\ =\left[Y(\xi),\ \frac{\mathrm{d}}{\mathrm{d}\xi}Y(\xi),\ \overline{D}(\xi)\frac{\mathrm{d}^2}{\mathrm{d}\xi^2}Y(\xi),\ \frac{\mathrm{d}}{\mathrm{d}\xi}\left[\overline{D}(\xi)\frac{\mathrm{d}^2}{\mathrm{d}\xi^2}Y(\xi)\right]\right]^{\mathrm{T}}$, Eq. (B2) becomes a set of the first order ordinary differential equations, expressed as

$$\frac{\mathrm{d}}{\mathrm{d}\xi}\boldsymbol{\theta}=\mathbf{A}(\xi)\cdot\boldsymbol{\theta}, \tag{B3}$$

where the coefficient matrix $\mathbf{A}$ is

$$\mathbf{A}(\xi)=\begin{bmatrix}0 & 1 & 0 & 0\\ 0 & 0 & \dfrac{1}{\overline{D}(\xi)} & 0\\ 0 & 0 & 0 & 1\\ \omega^2\overline{h}(\xi) & 0 & \dfrac{\overline{T}}{\overline{D}(\xi)} & 0\end{bmatrix}, \tag{B4}$$

where ω is the eigenfrequency of the system to be determined. Equation (B3) is a set of the variable coefficient equations. To solve this, the beam is divided into N segments along x-axis. The dimensionless length of each segment is $d\ =\ \xi_i-\xi_{i-1}\ =\ 1/N$, where $\xi_i\ =\ i/N$, for $i\ =\ 0,\ 1,\ 2,\ \ldots,\ N$. Approximately, in each segment, the beam is treated as a uniform one. At the k-th segment, the thickness of beam is $\overline{h}_k\ =\ \overline{h}\left(\frac{2k-1}{2N}\right)$. Equation (B3) becomes the following equations:

$$\frac{d}{d\xi}\boldsymbol{\theta}=\mathbf{A}_k\cdot\boldsymbol{\theta},\ (\xi_{k-1}\leqslant\xi\leqslant\xi_k,\ k=1,\ 2,\ 3\cdots N) \tag{B4}$$

where $\mathbf{A}_k\ =\mathbf{A}\left(\frac{2k-1}{2N}\right)$. Based on the ordinary differential equation theory [60], the solution for Eq. (B4) is $\boldsymbol{\theta}(\xi)\ =e^{\mathbf{A}_k\cdot(\xi-\xi_{k-1})}\boldsymbol{\theta}(\xi_{k-1})$, with $\xi_{k-1}\leqslant\xi\leqslant\xi_k$, $k\ =\ 1,\ 2,\ 3,\ \ldots N$. Let $\xi\ =\ \xi_k$ and then the solution becomes

$$\boldsymbol{\theta}(\xi_k)=e^{\mathbf{A}_k\cdot d}\boldsymbol{\theta}(\xi_{k-1}). \tag{B5}$$

For the continuity of the state vector $\boldsymbol{\theta}(\xi)$ along ξ, combining all the solutions of Eq. (B5) with $k = 1, 2, \ldots N$ gives the transfer relationship of the state vector between the two sides of beam [61]:

$$\boldsymbol{\theta}(1)=\prod_{i=1}^{N}e^{\mathbf{A}_{N+1-i}\cdot d}\boldsymbol{\theta}(0). \tag{B6}$$

The matrix exponential can be obtained by the Padé approximation [62,63]. The boundary conditions of Eqs. (A6) and (A7) can be rewritten in the following matrix form:

$$\mathbf{B}_0\boldsymbol{\theta}(0)+\mathbf{B}_1\boldsymbol{\theta}(1)=0, \tag{B7}$$

where $\mathbf{B}_0$ and $\mathbf{B}_1$ are given as follows:

For a cantilevered beam,

$$\boldsymbol{B}_0=\begin{bmatrix}1 & 0 & 0 & 0\\ 0 & 1 & 0 & 0\\ 0 & 0 & 0 & 0\\ 0 & 0 & 0 & 0\end{bmatrix},\boldsymbol{B}_1=\begin{bmatrix}0 & 0 & 0 & 0\\ 0 & 0 & 0 & 0\\ 0 & 0 & 1 & 0\\ 0 & -\overline{T} & 0 & 1\end{bmatrix}. \tag{B8}$$

For a doubly clamped beam,

$$\mathbf{B}_0=\begin{bmatrix}1 & 0 & 0 & 0\\ 0 & 1 & 0 & 0\\ 0 & 0 & 0 & 0\\ 0 & 0 & 0 & 0\end{bmatrix},\mathbf{B}_1=\begin{bmatrix}0 & 0 & 0 & 0\\ 0 & 0 & 0 & 0\\ 1 & 0 & 0 & 0\\ 0 & 1 & 0 & 0\end{bmatrix}. \tag{B9}$$

The matrix $\mathbf{B}_0$ and $\mathbf{B}_1$ represent the boundary conditions expressed by Eqs. (A6) and (A7). Substituting Eq. (B6) into Eq. (B7) gives the following

equations:

$$\left(\boldsymbol{B}_0+\boldsymbol{B}_1\prod_{i=1}^{N}\mathrm{e}^{\boldsymbol{A}_{N+1-i}\cdot d}\right)\boldsymbol{\theta}(0)=0. \tag{B10}$$

The eigenfrequency ω in Eq. (B10) is obtained by setting the following matrix determinant zero in order to have the nontrivial solution of $\boldsymbol{\theta}(0)$:

$$\det\left(\boldsymbol{B}_0+\boldsymbol{B}_1\prod_{i=1}^{N}\mathrm{e}^{\boldsymbol{A}_{N+1-i}\cdot d}\right)=0, \tag{B11}$$

where det() is the determinant of the matrix. The mode shape of beam vibration can be obtained numerically by repeating $\boldsymbol{\theta}(\xi_k)=\prod_{i=1}^{k}\mathrm{e}^{\boldsymbol{A}_{k+1-i}}\boldsymbol{\theta}(0)$ with increasing k from 1 to N.

Appendix C. Proof of the self-adjointness

The vibration of the variable thickness beam can be described by the governing equation:

$$BY(\xi)=\frac{\mathrm{d}^2}{\mathrm{d}\xi^2}\left[\overline{D}(\xi)\frac{\mathrm{d}^2Y(\xi)}{\mathrm{d}\xi^2}\right]-\overline{T}\frac{\mathrm{d}^2Y(\xi)}{\mathrm{d}\xi^2}=\lambda\overline{h}(\xi)Y(\xi). \tag{C1}$$

where B and λ are the differential operator and eigenvalue, respectively. The boundary conditions are concluded as follows:

$$\textit{Free end}: \overline{D}\frac{d^2Y}{d\xi^2}=0,\frac{d}{d\xi}\left[\overline{D}\frac{d^2Y}{d\xi^2}\right]-\overline{T}\frac{dY}{d\xi}=0; \tag{C2}$$

$$\textit{Clamped end}: Y=0,\frac{d}{d\xi}Y=0. \tag{C3}$$

The inner product of BY_i and Y_j is expressed as

$$\langle BY_i,Y_j\rangle=\int_0^1\left\{\frac{\mathrm{d}^2}{\mathrm{d}\xi^2}\left[\overline{D}(\xi)\frac{\mathrm{d}^2Y_i(\xi)}{\mathrm{d}\xi^2}\right]-\overline{T}\frac{\mathrm{d}^2Y_i(\xi)}{\mathrm{d}\xi^2}\right\}Y_j(\xi)\mathrm{d}\xi. \tag{C4}$$

The difference of $\langle BY_i,Y_j\rangle$ and $\langle BY_j,Y_i\rangle$ is as follows:

$$\langle BY_i,Y_j\rangle-\langle BY_j,Y_i\rangle=\left\{\frac{\mathrm{d}}{\mathrm{d}\xi}\left[\overline{D}\frac{\mathrm{d}^2Y_i}{\mathrm{d}\xi^2}\right]Y_j-\frac{\mathrm{d}}{\mathrm{d}\xi}\left[\overline{D}\frac{\mathrm{d}^2Y_j}{\mathrm{d}\xi^2}\right]Y_i\right\}\Big|_0^1-\overline{T}\left[\frac{\mathrm{d}Y_i}{\mathrm{d}\xi}Y_j-\frac{\mathrm{d}Y_j}{\mathrm{d}\xi}Y_i\right]\Big|_0^1-\left\{\left[\overline{D}\frac{\mathrm{d}^2Y_i}{\mathrm{d}\xi^2}\right]\frac{\mathrm{d}Y_j}{\mathrm{d}\xi}-\left[\overline{D}\frac{\mathrm{d}^2Y_j}{\mathrm{d}\xi^2}\right]\frac{\mathrm{d}Y_i}{\mathrm{d}\xi}\right\}\Big|_0^1 \tag{C5}$$

By substituting the boundary conditions of Eqs. (C2) or (C3) into Eq. (C5) becomes:

$$\langle BY_i,Y_j\rangle-\langle BY_j,Y_i\rangle=0 \tag{C6}$$

Thus, the operator of Eq. (C1) is self-adjoint.

Appendix D. Curve-fitting of the optimized shapes

The optimal shapes of the optimized cantilevers are curve-fitted as the following polynomial functions for the first ($j=1$) and second ($j=2$) modes:

$$\begin{cases}\overline{h}(\xi)=2-0.138\xi-8.366\xi^2+15.348\xi^3-15.265\xi^4+6.440\xi^5, & (j=1),\\ \overline{h}(\xi)=\begin{cases}1.914-1.060\xi-55.048\xi^2+412.565\xi^3-1606.311\xi^4+1956.275\xi^5, & \xi\leqslant 0.25\\ -7.685+69.201\xi-225.695\xi^2+387.464\xi^3-338.655\xi^4+115.417\xi^5, & \xi\geqslant 0.25\end{cases} & (j=2).\end{cases} \tag{D1}$$

The optimal shapes of the optimized doubly clamped beams are curve-fitted as follows:

$$\begin{cases}\overline{h}(\xi)=1.979+1.515\xi-38.419\xi^2+73.808\xi^3-36.904\xi^4, (j=1),\\ \overline{h}(\xi)=\begin{cases}1.796-1.628\xi+271.487\xi^2+13152\xi^3-155648\xi^4-591710\xi^5, & \xi<0.113\\ 4.557-1.002E3\xi-9.096E3\xi^2-3.525E3\xi^3+6.532E3\xi^4-5.724E3\xi^5+1.908E3\xi^6, & 0.113\leqslant\xi\leqslant 0.887\\ -4.489E5+2.375E6\xi-5.022E6\xi^2+5.308E6\xi^3-2.803E6\xi^4-5.917E5\xi^5, & \xi>0.113\end{cases} & (j=3).\end{cases} \tag{D2}$$

References

[1] Dominguez-Medina S, Fostner S, Defoort M, Sansa M, Stark A-K, Halim MA, et al. Neutral mass spectrometry of virus capsids above 100 megadaltons with nanomechanical resonators. Science 2018;362(6417):918–22.

[2] Jalil J, Zhu Y, Ekanayake C, Ruan Y. Sensing of single electrons using micro and nano technologies: a review. Nanotechnology 2017;28:142002.

[3] Shekhawat GS, Dravid VP. Applied physics: nanoscale imaging of buried structures via scanning near-field ultrasound holography. Science 2005;310(5745):89–92.

[4] Zhang Y. Detecting the stiffness and mass of biochemical adsorbates by a resonator sensor. Sens Actuator B Chem 2014;202:286–93.

[5] Jaber N, Ilyas S, Shekhah O, Eddaoudi M, Younis MI. Multimode MEMS resonator for simultaneous sensing of vapor concentration and temperature. IEEE Sens J 2018;18(24):10145–53.
[6] Xu Y, Lin JT, Alphenaar BW, Keynton RS. Viscous damping of microresonators for gas composition analysis. Appl Phys Lett 2006;88:143513.
[7] Li J, Gai L, Li H, Hu H. A high sensitivity temperature sensor based on packaged microfibre knot resonator. Sens Actuator A Phys 2017;263:369–72.
[8] Sage E, Brenac A, Alava T, Morel R, Dupré C, Hanay MS, et al. Neutral particle mass spectrometry with nanomechanical systems. Nat Commun 2015;6(1).
[9] Wiltshire BD, Mirshahidi K, Nadaraja AV, Shabanian S, Hajiraissi R, Zarifi MH, et al. Oleophobic textiles with embedded liquid and vapor hazard detection using differential planar microwave resonators. J Hazard Mater 2021;409:124945.
[10] Janshoff A, Galla H-J, Steinem C. Piezoelectric mass-sensing devices as biosensors – an alternative to optical biosensors? Angew Chem Int Ed 2000;39(22):4004–32.
[11] Zhao J, Wang L, Fu D, Zhao D, Wang Y, Yuan Q, et al. Gold nanoparticles amplified microcantilever biosensor for detecting protein biomarkers with high sensitivity. Sens Actuator A Phys 2021;321:112563.
[12] Peng HB, Chang CW, Aloni S, Yuzvinsky TD, Zettl A. Ultrahigh frequency nanotube resonators. Phys Rev Lett 2006;97:87203.
[13] Huang XMH, Zormant CA, Mehreganyt M, Roukes ML. Nanoelectromehanical systems: Nanodevice motion at microwave frequencies. Nature 2003;421:496.
[14] Burg TP, Godin M, Knudsen SM, Shen W, Carlson G, Foster JS, et al. Weighing of biomolecules, single cells and single nanoparticles in fluid. Nature 2007;446 (7139):1066–9.
[15] Roukes M. Nanoelectromechanical systems face the future. Phys World 2001;14(2): 25–32.
[16] Chiu H-Y, Hung P, Postma HWC, Bockrath M. Atomic-scale mass sensing using carbon nanotube resonators. Nano Lett 2008;8(12):4342–6.
[17] Boisen A, Dohn S, Keller SS, Schmid S, Tenje M. Cantilever-like micromechanical sensors. ep Prog Phys 2011;74(3):036101.
[18] Arlett JL, Myers EB, Roukes ML. Comparative advantages of mechanical biosensors. Nat Nanotechnol 2011;6(4):203–15.
[19] Schmid S, Villanueva LG, Roukes ML. Fundamentals of nanomechanical Resonators, vol. 49. Springer; 2016.
[20] Timoshenko S. Vibration problems in engineering. 4th ed. New York: Wiley; 1974.
[21] Duan Ke, Li Y, Li Li, Hu Y, Wang X. Diamond nanothread based resonators: ultrahigh sensitivity and low dissipation. Nanoscale 2018;10(17):8058–65.
[22] Hu H, Cho H, Somnath S, Vakakis AF, King WP. Silicon nano-mechanical resonators fabricated by using tip-based nanofabrication. Nanotechnology 2014; 25:275301.
[23] Lifshitz R, Roukes ML. Thermoelastic damping in micro- and nanomechanical systems. Phys Rev B 2000;61(8):5600–9.
[24] Ghaffari S, Chandorkar SA, Wang S, Ng EJ, Ahn CH, Hong V, et al. Quantum limit of quality factor in silicon micro and nano mechanical resonators. Sci Rep 2013;3 (1).
[25] Ekinci KL, Yang YT, Roukes ML. Ultimate limits to inertial mass sensing based upon nanoelectromechanical systems. J Appl Phys 2004;95(5):2682–9.
[26] Tamayo J. Study of the noise of micromechanical oscillators under quality factor enhancement via driving force control. J Appl Phys 2005;97(4):044903.
[27] Page M, La Fontaine J, Chen X, Zhao C, Ju L, Blair D, et al. Ultra-low dissipation resonators for improving the sensitivity of gravitational wave detectors. Phys Lett A 2018;382(33):2174–80.
[28] Ghatkesar MK, Barwich V, Braun T, Ramseyer JP, Gerber C, Hegner M, et al. Higher modes of vibration increase mass sensitivity in nanomechanical microcantilevers. Nanotechnology 2007;18:445502.
[29] Jin D, Li X, Liu J, Zuo G, Wang Y, Liu M, et al. High-mode resonant piezoresistive cantilever sensors for tens-femtogram resoluble mass sensing in air. J Micromech Microeng 2006;16(5):1017–23.
[30] Nguyen LQ, Larsen PE, Bishnoi S, Boisen A, Keller SS. Fabrication of fully suspended pyrolytic carbon string resonators for characterization of drug nano-and microparticles. Sens Actuator A Phys 2019;288:194–203.
[31] Kim S-B, Kim J-H. Quality factors for the nano-mechanical tubes with thermoelastic damping and initial stress. J Sound Vib 2011;330(7):1393–402.
[32] Wei X, Chen Q, Xu S, Peng L, Zuo J. Beam to string transition of vibrating carbon nanotubes under axial tension. Adv Funct Mater 2009;19(11):1753–8.
[33] Zhang Y, Zhao YP. Mass and force sensing of an adsorbate on a string resonator. Sens Actuator B Chem 2015;221:305–11.
[34] Wei C, Zhang Y. Mass identification of multiple particles on a doubly clamped resonator. Sens Actuator B Chem 2022;360:131682.
[35] Spletzer M, Raman A, Wu AQ, Xu X, Reifenberger R. Ultrasensitive mass sensing using mode localization in coupled microcantilevers. Appl Phys Lett 2006;88: 254102.
[36] Gao R, Huang Yu, Wen X, Zhao J, Liu S. Method to further improve sensitivity for high-order vibration mode mass sensors with stepped cantilevers. IEEE Sens J 2017;17(14):4405–11.
[37] Hsu Y-L. A review of structural shape optimization. Comput Ind 1994;25(1):3–13.
[38] Dietl JM, Garcia E. Beam shape optimization for power harvesting. J Intell Mater Sys Struct 2010;21(6):633–46.
[39] Melli M, Pozzato A, Lazzarino M. Inverted tapered pillars for mass sensing. Microelectron Eng 2010;87(5-8):730–3.
[40] Joshi AY, Sharma SC, Harsha SP. Zeptogram scale mass sensing using single walled carbon nanotube based biosensors. Sens Actuator A Phys 2011;168(2):275–80.
[41] Grandhi R. Structural optimization with frequency constraints – a review. AIAA J 1993;31(12):2296–303.
[42] Hanagud S, Chattopadhyay A, Smith CV. Optimal design of a vibrating beam with coupled bending and torsion. AIAA J 1987;25(9):1231–40.
[43] Wang FY. Optimum design of vibrating cantilevers: a classical probem revisited. J Optim Theory Appl 1995;84(3):635–52.
[44] Meske R, Lauber B, Schnack E. A new optimality criteria method for shape optimization of natural frequency problems. Struct Multidiscip Optim 2006;31(4): 295–310.
[45] Banks HT, Inman DJ. On damping mechanisms in beams. J Appl Mech 1991;58: 716–23.
[46] Wasisto HS, Merzsch S, Waag A, Uhde E, Salthammer T, Peiner E. Airborne engineered nanoparticle mass sensor based on a silicon resonant cantilever. Sens Actuator B Chem 2013;180:77–89.
[47] Ma Z-D, Kikuchi N, Hagiwara I. Structural topology and shape optimization for a frequency response problem. Comput Mech 1993;13(3):157–74.
[48] Haslinger J, Mäkinen RAE. Introduction to shape optimization. Philadelphia: SIAM; 2003.
[49] Byrd RH, Hribar ME, Nocedal J. An interior point algorithm for large-Scale nonlinear programming. SIAM J Optim 1999;9(4):877–900.
[50] Mehdipour I, Barari A. Why the center-point of bridged carbon nanotube length is the most mass sensitive location for mass attachment? Comput Mater Sci 2012;55: 136–41.
[51] Ali-Akbari HR, Shaat M, Abdelkefi A. Bridged single-walled carbon nanotube-based atomic-scale mass sensors. Appl Phys A Mater Sci Process 2016;122:762.
[52] Wang Ji, Shen L, Yang J. Effects of electrodes with continuously varying thickness on energy trapping in thickness-shear mode quartz resonators. Ultrasonics 2008;48 (2):150–4.
[53] Li X-F, Kang Y-A, Wu J-X. Exact frequency equations of free vibration of exponentially functionally graded beams. Appl Acoust 2013;74(3):413–20.
[54] Wang Z, Wang X, Xu G, Cheng S, Zeng T. Free vibration of two-directional functionally graded beams. Compos Struct 2016;135:191–8.
[55] Dohn S, Sandberg R, Svendsen W, Boisen A. Enhanced functionality of cantilever based mass sensors using higher modes. Appl Phys Lett 2005;86:1–3.
[56] Dohn S, Svendsen W, Boisen A, Hansen O. Mass and position determination of attached particles on cantilever based mass sensors. Rev Sci Instrum 2007;78: 103303.
[57] Calderon Hurtado A, Peralta P, Ruiz RO, Makki Alamdari M, Atroshchenko E. Shape optimization of piezoelectric energy harvesters of variable thickness. J Sound Vib 2022;517:116503.
[58] Meirovitch L. Analytical methods in vibrations. New York: Macmillan; 1967.
[59] Guenther RB, Lee JW. Sturm-Liouville problems: theory and numerical implementation. Boca Raton: CRC Press; 2019.
[60] Esquembre F, Christian W. Ordinary differential equations. 2nd ed. Philadelphia: Society for Industrial and Applied Mathematics; 2007.
[61] Wei C, Shang X. Analysis on nonlinear vibration of breathing cracked beam. J Sound Vib 2019;461:114901.
[62] Moler C, Van Loan C. Nineteen dubious ways to compute the exponential of a matrix. SIAM Rev 1978;20(4):801–36.
[63] Moler C, Van Loan C. Nineteen dubious ways to compute the exponential of a matrix, twenty-five years later. SIAM Rev 2003;45(1):3–49.